Energy management controller for fuel cell hybrid electric vehicle based on sat-nav data

Al-sagheer, Yousif; Steinberger-Wilckens, Robert

DOI:
10.1002/fuce.201900196

Fuel Cells

Energy Management Controller for Fuel Cell Hybrid Electric Vehicle Based on Sat-Nav Data

Journal:	*Fuel Cells*
Manuscript ID	fuce.201900196.R2
Wiley - Manuscript type:	Original Research Paper
Date Submitted by the Author:	24-Feb-2020
Complete List of Authors:	Al-Sagheer, Yousif; University of Birmingham, School of Chemical Engineering; University of Birmingham, Chemical Engineering Steinberger-Wilckens, Robert; University of Birmigham, Chemical Engineering
Keywords:	Battery Electric Vehicle, Fuel Cells, Fuel Cell Systems, Fuel Cell Hybrid Electric Vehicle, Power Split Control, Fuel Cell Power Control, DC-DC Converter, Electric Powertrain Control, Energy Management.

Energy Management Controller for Fuel Cell Hybrid Electric Vehicle Based on Sat-Nav Data

Y. Al-Sagheer[1,*], R. Steinberger-Wilckens[1]

[1]Birmingham Centre for Fuel Cell and Hydrogen Research, University of Birmingham, B15 2TT, United Kingdom

[*] Corresponding author: Y.I.W.Al-Sagheer@bham.ac.uk

Abstract

The hybridisation of fuel cells (FC) and battery in electric vehicles necessitates designing an energy management system (EMS) for optimal energy use of the two power sources. The EMS represents a high-level controller (HLC) calculating the optimal power split between the two power sources, using a prediction model for the vehicle's electric load over a planned journey trajectory. However, the instantaneous actual power demand of the vehicle is likely to deviate from the prediction due to varying traffic circumstances. This power offset needs to be compensated for whilst the optimality is still considered. A control approach is proposed here that converts the optimal power split into a dimensionless power split ratio (PSR). This ratio is passed to a low-level controller (LLC) to be implemented as a set-point. The LLC is responsible for simultaneously controlling the power of the FC and the battery using solely one control element, which is the DC-DC boost converter. The PSR will be maintained whatever the actual power demand of the vehicle is. This approach will result in a fully controlled optimal power utilisation so that the high efficiency of the battery and the extended range enabled by the FC system are used to best effect.

Keywords: Battery Electric Vehicle, Fuel Cells, Fuel Cell Systems, Fuel Cell Hybrid Electric Vehicle, Power Split Control, Fuel Cell Power Control, DC-DC Converter, Electric Powertrain Control, Energy Management.

1 Introduction

Hydrogen is the energy vector for the future and will play an important role in decarbonising the transport sector and many other industries. The efficiency of fuel cell powertrains is questionable in comparison to pure battery electric powertrains [1]. However, fuel cell vehicles (FCV) have the advantage of extended range and zero emissions when green hydrogen gas is the fuel.

In the automotive industry, reducing emissions from vehicles has become an important challenge. Worsening urban air quality and the global impacts of CO_2 have put pressure on governments to introduce legislation such as the EURO VI, which aims to significantly reduce pollution from vehicles [2]. One solution is the electrification of vehicles such as hybrid electric vehicles (HEV), battery electric vehicles (BEV), plug-in hybrid electric vehicles (PHEV), and fuel cell hybrid electric vehicles (FCHEV) [3,4]. These technologies are important due to their low or zero exhaust emissions and potential to reduce or eliminate the use of diminishing fossil fuel supplies [5]. FCHEVs are a technology of particular interest as the battery and fuel cell (FC) can work together, efficiently, to extend the driving range and provide the advantages of hybridisation such as: regenerative breaking, improvement of transient power demand, and ability to optimise the vehicle performance [6].

In FCHEVs the FC and the battery can run independently or together to supply the power to the vehicle. When there are two energy sources this can lead to a complicated power flow, which requires an advanced energy management system (EMS). The aim of this investigation was to design a high-level EMS capable of maximising vehicle efficiency within a number of constraints while maintaining drivability. In FCHEVs, the high-level energy management problem often requires information of the state of charge (SoC) of the battery and the hydrogen inventory to determine the optimal power split between the FC and battery. Model predictive control (MPC) is one control strategy capable of using a prediction of the future driving

conditions with a SoC plan to achieve optimal energy use for a FCHEV [7]. The predictive aspect and the ability of an MPC to handle uncertainty is why it was chosen for the proposed EMS.

Most of the previous work in literature has tested specific research methodologies by finding the optimal power split for a pre-defined drive cycle. In the real world, a known drive cycle would not be available unless after finishing the journey of the vehicle. Obviously, such approaches undergo loss of optimality conditions when the real circumstances during driving do not match with the proposed drive cycle. In short, the uncertainty of the drive cycle prediction is not considered in these approaches. The MPC algorithm in this study seeks to find the optimal power split between the fuel cell and the battery based on the economic value of energy while respecting the operational constraints of power and energy for these two energy sources.

2 Scientific Approach

The energy management in this study is implemented by a model predictive control (MPC) algorithm, as a model-based approach. The MPC algorithm is applied to find the optimal power split between the FC stack and the battery over a planned trip from point A to point B, considering the energy inventory on-board the vehicle for both hydrogen tank and the SOC of the battery, and also considering any operational constraints. The EMS was simulated on the LabVIEW platform using multiple LabVIEW vi loops to mimic the powertrain components and apply the MPC algorithm. In LabVIEW, each loop can run at different sampling time and the synchronisation of input and output data to and from these loops is achieved using LabVIEW global variables. This approach enables the simulation to run each model independently from others. For example, the power split controller is required to run at a high sampling rate that is close to real-time control. While updating, the Sat-Nav data could be read at a far lower rate.

Figure 1 explains the simulation architecture for this study. The LabVIEW global variables pool is accessible to all other vi loops and each loop can read and write from and to the pool to update the simulation results. This approach will facilitate later substituting each loop with its corresponding input/output data from real-world hardware units ('hardware in the loop'). For example, the LabVIEW loop that simulates the hydrogen tank can be removed and substituted by real-world measurements of hydrogen usage and tank content. Obviously, this will require introducing a new vi loop that measures the hydrogen flow rate and hydrogen tank pressure.

The required prediction models for the MPC algorithm are vehicle model, route model, hydrogen tank model, and the battery model.

2.1 Vehicle Model

This is a mathematical model that predicts power demand of the vehicle as a function of vehicle speed, acceleration, and road gradient. The model also includes design parameters of the vehicle such as the mass, aerodynamic drag area, etc. and the combination of all forces exerted on the vehicle system [8,9], as described in Eqs. (1-5) below.

$$P_v(t) = (F_{aero} + F_{grade} + F_{rr} + F_i)\, v(t) \quad (1)$$

and

$$F_{aero} = 0.5\, \rho C_d A_f v^2(t) \quad (2)$$

$$F_{grade} = mgsin(\theta) \quad (3)$$

$$F_{rr} = mgC_{rr} \quad (4)$$

$$F_i = ma \quad (5)$$

where, F_{aero}, F_{grade}, F_{rr}, and F_i are the aerodynamic, gradient, rolling and acceleration resistances, respectively. ρ is the air density, $C_d A_f$ is the drag area, $v(t)$ is the vehicle velocity, m is the vehicle mass, g is the gravitational acceleration, θ is the road gradient, C_{rr} is the rolling

resistance coefficient, and *a* is the vehicle acceleration. A LabVIEW model, Figure 2, is used for predicting the power and energy demand for each route segment.

For the purpose of the simulation, another LabVIEW loop is required to simulate a real-time motor load measurement, which will vary according to vehicle acceleration, speed, and traffic conditions.

2.2 Route Model

The Sat-Nav data provides an estimation of the total distance of the current trip and the number of the route segments with their distances and gradients. It can also provide a recommended speed on each route segment depending on whether travel is in an urban area or on the motorway. The Sat-Nav data can be obtained from a map service such as Open Street Map, or any third-party service such as EV trip planner [10].

In order to distinguish between what is certain and what is uncertain in the prediction, route segment distances are considered as certain data as they are geographical information. The best estimation for the time required to pass each segment is assumed to be based on traffic regulations. However, the actual speed will be subject to driver behaviour and accordingly, the power requirement also depends on this. Figure 3 shows the power of the vehicle when it accelerates from rest to a speed of 60 miles per hour (~27 m s^{-1}). The higher the acceleration, the higher the load on the electric machine of the vehicle. When the desired speed is attained, no acceleration power will be required, hence the power requirement will be limited to overcome aerodynamic, gradient, and rolling resistances. Therefore, maintaining the vehicle at a constant speed of 27 m s^{-1} will require the same amount of power whatever the acceleration was followed to attain this speed.

The huge difference between power spikes due to acceleration and the steady state power required to maintain a constant speed justifies the need of hybridisation of the powertrain. The

size of the fuel cell could be chosen to fulfill the energy supply at steady state vehicle speed, while transient peaks could be supplied by transient power sources like a supercapacitor and/or a battery. The hybridisation with a FC stack will offer an extended range for the powertrain system due to the ability of storing a high amount of fuel owing to the high gravimetric energy density of hydrogen [11].

2.3 Fuel Cell

The polymer electrolyte fuel cell (PEFC) voltage and power are modelled by a well-known formula in the literature, which is the FC polarisation curve [12,13]. This formula describes the FC voltage in terms of the Nernst potential and FC losses that are functions of FC current, Eqs. (6-7).

$$V_{FC} = N_{cell}\left[E_{Nernst} - \eta_{act} - \eta_{ohm} - \eta_{conc}\right] \quad (6)$$

$$P_{FC} = V_{FC} \cdot I_{FC} \quad (7)$$

FC stack efficiency can also be expressed in terms of hydrogen thermoneutral potential and the actual stack output voltage, Eq. (8).

$$\eta_{\mathrm{FC}} = \frac{V_{FC}}{1.48 \times N_{cell}} \quad (8)$$

2.4 The Battery

A discrete power integrator model is used for modelling the state of charge (SoC) of a lithium-ion battery [14,15]. The battery model is implemented using a separate integral loop with a sampling time of 50ms independent from other loop sampling times. A change in SoC is calculated by the balance of battery charging energy (negative) or discharging energy (positive) to the battery Watt-hours capacity, as shown in Eqs. (9-10).

$$\mathrm{SoC}^{k+1} = \mathrm{SoC}^{k} - \frac{\alpha\, P_B^k\ t_{s7}}{3600\ C_{Wh}} \quad (9)$$

$$\alpha = \begin{cases} 1/\eta_{dis} & P_B > 0 \\ \eta_{ch} & P_B < 0 \end{cases} \quad (10)$$

The battery efficiency is a function of the battery temperature, charging or discharging load, and the current SoC [16,17]. An average charge and discharge efficiency of 0.98 and 0.99 are assumed, respectively [18,19].

For the MPC algorithm, the SoC is mapped over the prediction horizon by Eq. (11) depending on the battery power usage and the estimated time intervals t^i required to travel across road segments. Battery efficiency is not considered in Eq. (11) in order to simplify the design of the controller and since the battery efficiency depends on the direction of battery power flow. Power supplied by the battery is an optimisation variable in this case and is required to retain the linear form of the optimisation problem.

$$\mathrm{SoC}^i = \mathrm{SoC}^0 - \sum_i^N \frac{P_B^i \; t^i}{3600 \; C_{Wh}} \quad (11)$$

2.5 H_2 Tank

Hydrogen gas status in moles is modelled by another LabVIEW integral loop depending on FC electrical current.

$$M_{\mathrm{H_2}}^{k+1} = M_{\mathrm{H_2}}^{k} - \frac{N_{cell}\, I_{FC}^k\, t_{s3}}{2F} \quad (12)$$

For the MPC algorithm, the hydrogen tank inventory over the prediction horizon is estimated as a function of FC power, the higher heating value of hydrogen, the average FC efficiency, and the estimated time intervals, as in Eq. (13).

$$M_{\mathrm{H_2}}^{i} = M_{\mathrm{H_2}}^{0} - \sum_i^N \frac{P_{FC}^i \; t^i}{\eta_{FC}\, \Delta H_{\mathrm{H_2}}} \quad (13)$$

The accuracy of estimate for the SoC and hydrogen inventory at any point of car journey depends on the accuracy of the time intervals estimated for road segments. Therefore, a detailed Sat-Nav data set will enable the controller to make better decisions to improve the energy management. Nevertheless, the detailed and prolonged Sat-Nav data will add computational burden due to an increase of optimisation variable number, hence, a more powerful computer processors are required.

3 FCHEV Powertrain

The powertrain of the vehicle consists of the fuel cell stack and the battery pack. These two power sources are connected to a DC bus through which power is supplied to the vehicle's electric motor. Figure 4 shows the design of the proposed powertrain of the FCHEV. The driver controls the speed or the torque of the motor by a DC/AC inverter. Therefore, the real power demand will depend heavily on driving behaviour and driver attitude following real-world traffic.

The fuel cell delivers an unregulated voltage according to the polarisation curve of the stack, and therefore a power conditioning stage is required to control the voltage of the FC power delivered to the DC bus. The DC-DC boost converter interfaces the FC terminals with the other powertrain components. The converter can operate in three control modes, which are voltage-mode control, voltage-mode with current limit control, and current-mode control. In this study, the converter is selected to operate in current-mode control to regulate the FC power.

It should be noted that not only the boost converter can control the power balance on the DC bus. The motor control unit, which could be a bi-directional inverter, can regulate regenerative power of the motor during vehicle deceleration and breaking events. In these events, the motor will act as an energy source and the inverter can play the role of a second control element to regulate the charging process of the battery or a supercapacitor. A comprehensive control

strategy for these two control elements will provide full controllability of the energy flow across the DC bus. However, the role of the inverter as a regenerative controller is not considered in this study, and the proposed design aims only to investigate and introduce add-on control capabilities for the DC-DC boost converter.

4 Power Split Controller

In order to implement an FCHEV EMS, a power split controller (PSC) is required to control the power output from the fuel cell and the battery simultaneously. The overall control system comprises of multi-level of control. That includes a low-level control (LLC) responsible for controlling FC load with respect to the battery load and a supervisory high-level control (HLC) responsible for the EMS. The LLC applies a novel control approach developed under UK Patent Application No. 1903895.9

The LLC power split controller has been tested experimentally by prototyping the novel approach on the LabVIEW platform using the National Instruments NI PXI-8105 embedded controller with NI PXI-6259 DAQ-card. The performance of the LLC against different power set points for the FC and the battery is shown in Figure 5. The FC and the battery power set points are attained very well and maintained so that the sum of power from the two sources is equal to the motor load, provided that these powers are subject to power electronic losses. Zero battery contribution to the motor load can be achieved when it is required and decided by the EMS. Also, positive and negative power (discharging and charging) of the battery can be controlled effectively and more importantly using only one control element, which is the DC-DC converter of the FC. The converter used in this prototype is a boost converter operating in current-control mode. A detailed description of the PSC with the novel control approach will be published subsequently.

5 Range Extender

The plug-in feature of the powertrain decides which one of the power sources will act as a range extender. For plug-in FCHEVs, the battery can be charged from an external power source, such as the grid, during car parking time at night. Such external power source will be a cheaper source of energy and therefore the priority of power supply would be preferred to be from the battery rather than from the fuel cell, which will then be considered as the range extender in this case. While for a non-plug-in configuration, the main and only energy source on-board the vehicle will be the FC stack which provides energy for the motor load demand plus providing charging energy for the battery when required. Hence, the battery will be the range extender in this case. In this paper, a plug-in powertrain configuration is considered and upon that the control objectives are designed to reflect the energy supply priority of the battery over the FC.

6 Model Predictive Control (MPC)

MPC is an advanced and flexible control algorithm which makes use of a process model to find the optimal trajectory of control moves over a prediction horizon. Formulating an MPC control problem starts with defining a cost function consisting of pre-defined performance indices or control objectives. Finding the optimal minima of the cost function subject to operational and safety constraints results in control moves that provide optimal system performance while respecting the limits defined by the constraints [20].

A supervisory high-level controller (HLC) is needed to calculate the power set points for the LLC for the FC and the battery. The HLC is based on an MPC algorithm to calculate the optimal power split between the two power sources. The MPC adopts a feedforward principle by predicting the power and energy requirements of the vehicle. An important issue that requires attention in designing the controller is the uncertainty of the prediction. The uncertainty has been dealt with in this work by converting the optimal power split between the fuel cell and the battery into an optimal power split ratio (PSR). The PSR will be implemented and sustained by

the LLC, taking into account the offset for a deviation between power prediction and instantaneous real load demand of the vehicle. This approach of collaboration between the HLC and LLC will result in a novel adaptation of optimality control that is subject to uncertainty of the vehicle model and the Sat-Nav data. Figure 6 shows a diagram of the proposed energy management controller. The control element in this configuration is the DC-DC boost converter of the FC. The converter is controlled directly by the LLC using a current-control mode of the converter that regulates the input current, which is the FC stack DC output current. The LLC and HLC are interconnected in a master/slave hierarchy.

7 Cost Function and Constraints

The design of the MPC controller starts with constructing a cost function with constraints. The cost function and the constraints are required to be represented in terms of control variables P_{FC} and P_{Bat}. Linear and simplified formula for the cost function and the constraints are preferred so that a linear solver can be used. The cost function consists of performance indices that penalise the deviation from a trajectory of load demand prediction for the vehicle, also consisting of performance indices that provide costing of supplying power from each of the two power sources. In this study, the proposed cost function contains four performance indices shown in Eq. (14).

$$\mathbf{min}\, J = \sum_{i=1}^{N} \left[w_1 \left(P_{v*}^{k+i} - \eta_c \cdot P_{FC}^{k+i} \right)^2 + w_2 \left(P_{v*}^{k+i} - P_B^{k+i} \right)^2 + w_3 \left(P_{FC}^{k+i} \right)^2 + w_4 \left(P_B^{k+i} \right)^2 \right] \tag{14}$$

where P_{v*}, P_{FC}, P_B are the vehicle, FC, and the battery power, respectively, and η_c, k, i, N are the DC-DC converter efficiency, the current sampling time, road segment number, and the total number of segments, respectively. w_1, w_2, w_3, w_4 are weighting factors of the performance indices which can be used for tuning the performance and shifting the control actions and the optimality towards the desired control objectives.

The third and fourth performance indices provide a relative preference of supplying power from the FC or from the battery. The weightings, w_3 and w_4, are based on the relative monetary costs of the two power sources. The comparative cost of running a FC and battery have been examined in [21]. The results of this investigation showed that the relative costs are likely to change with future cost reductions for FCs. However, for 2020 it is expected that for a midsize vehicle the operating cost of the FC and battery will be approximately 0.25 and 0.043 £ km^{-1}, respectively. The ratio of these costs is approximately 6:1, and this ratio is used for evaluating w_3 and w_4 so that they give preference to the use of the battery to minimise the cost function, unless the operation is outside of the constraints of the battery. The final weightings for the cost function are 1, 1, 6, 1, respectively.

The optimisation variables P_{FC} and P_B are forwarded to the LLC as set points for the FC stack and the battery. The minimisation of the cost function is subject to operational constraints which dictate the controller output to not violate defined safety and/or physical limits. The following constraints are applied:

$$P_B^{k+i} + \eta_c P_{FC}^{k+i} = P_{v*}^{k+i} \quad \text{(equality constraint)} \tag{15}$$

$$\left.\begin{aligned} 0 \le P_{FC}^{k+i} \le P_{FC}^{max} \\ P_B^{min} \le P_B^{k+i} \le P_B^{max} \\ M_{H_2}^{min} \le M_{H_2}^{k+i} \\ SoC^{min} \le SoC^{k+i} \le SoC^{max} \end{aligned}\right\} \quad \text{(inequality constraints)} \tag{16–19}$$

The equality constraint forces the optimisation process not to calculate power set points for the battery and FC that exceed the power demand of the vehicle. This is consistent with the fact that the load of the motor represents a physical limit for the combined FC and battery powers. The efficiency of the converter is included here because the FC is not directly contributing to DC load demand at the DC bus, hence converter losses have to be included.

The constraints in Eq. (16) define the physical limit of zero FC power, that is, FC power cannot be negative. Also, Eq. (16) provides a safety limit of maximum FC power. The constraints in

Eq. (17) provides safety limits of the battery discharging and charging power. Since the charging process is aimed to be controlled by another control element (not by the DC-DC boost converter of the FC), the constraint P_B^{min} is neglected in this study. The same is applicable to the constraint SoC^{max}. The constraints $M_{H_2}^{min}$ and SoC^{min} are aimed at defining the energy management for the energy assets on-board the vehicle.

The uncertainty of the power prediction is considered only for the current road segment where a measurement of motor electrical load is available. The uncertainty is compensated for by introducing an error term into the prediction model, as in Eq. (20).

$$\begin{aligned}\mathbf{min}\, J = \sum_{i=1}^{N}\Big\{ & w_1\Big[\left(P_{v*}^{k+i} + \varepsilon_{P_v}\right) - P_v^{id} - \eta_c \cdot P_{FC}^{k+i}\Big]^2 \\ & + w_2\Big[\left(P_{v*}^{k+i} + \varepsilon_{P_v}\right) + P_v^{id} - P_B^{k+i}\Big]^2 + w_3\left(P_{FC}^{k+i}\right)^2 + w_4\left(P_B^{k+i}\right)^2\Big\}\end{aligned} \tag{20}$$

where ε_{P_v} is the error of the prediction after a measurement of real vehicle load demand was available.

$$\varepsilon_{P_v} = P_v - P_{v*} \tag{21}$$

P_v^{id} is a term introduced to the cost function in order to shift the optimality toward supplying low levels of vehicle electrical load from the battery solely, for example, when the vehicle stops and its load is limited to the idle power of the vehicle auxiliaries [22]. Also, this term can be utilised to bias the priority of power supply toward the battery to avoid operating the FC at low power levels of the motor. Low power demand would likely result in the FC system to operate in a low system efficiency region, as shown in Figure 7.

It should be noted that the classical MPC algorithm applies the concept of receding horizon which moves a constant prediction horizon one step ahead at every sampling time [23]. This concept has been modified in this study. For our system of travelling vehicle, the open prediction horizon is not applicable because as the vehicle approaches the end of the trip the remaining road length gets shorter and therefore the road segments ahead are reduced. A

decreasing horizon is applied instead which is more realistic with the pre-defined Sat-Nav data acquired at the beginning of the journey. Thus, the size of the cost function decreases as well and therefore the computational burden is lightened with every route segment passed.

A linear quadratic programming solver is used for solving the cost function. The solving time of the optimisation step in the MPC defines the limits of sampling rate for the control loop. For the quadratic solver, the optimisation problem is required to be formulated in vectors and matrix notations. Eq. (20) can be re-written in vector notation as in Eq. (22)

$$\boldsymbol{J} = \frac{1}{2}\left[\vec{\boldsymbol{P}}_{\mathrm{FC}}\ ;\vec{\boldsymbol{P}}_{\mathrm{B}}\right]^{\mathrm{T}}\ \boldsymbol{H}\ \ \left[\vec{\boldsymbol{P}}_{\mathrm{FC}}\ ;\vec{\boldsymbol{P}}_{\mathrm{B}}\right] - \left[\vec{\boldsymbol{P}}_{\mathrm{FC}}\ ;\vec{\boldsymbol{P}}_{\mathrm{B}}\right]^{\mathrm{T}}\boldsymbol{f} \tag{22}$$

where $\boldsymbol{H}$ is the quadratic term matrix of Nx2N size, $\boldsymbol{f}$ is the linear vector term of the quadratic equation of size 2Nx1. $\left[\vec{\mathbf{P}}_{\mathrm{FC}}\ ,\vec{\mathbf{P}}_{\mathrm{B}}\right]$ is the optimal control trajectory of size 1x2N for the FC and the battery, respectively, as shown in Eq. (23).

$$\left[\vec{\boldsymbol{P}}_{\mathrm{FC}}\ ;\vec{\boldsymbol{P}}_{\mathrm{B}}\right] = \left[P_{\mathrm{FC}}^{k+1}\ P_{\mathrm{FC}}^{k+2}\ \cdots\ P_{\mathrm{FC}}^{k+N}\ \ P_{\mathrm{B}}^{k+1}\ \ P_{\mathrm{B}}^{k+2}\ \cdots\ P_{\mathrm{B}}^{k+N}\right]^{\mathrm{T}} \tag{23}$$

The vector notations of $\boldsymbol{H}$, $\boldsymbol{f}$, and the constraint are described in appendix A.

8 Results and Discussion

The response of the controller to operational constraints is shown in Figure 8. The threshold of vehicle power that the FC should start at was very well adhered to. A power threshold of 5 kW was selected here as an example to demonstrate the controller performance. Different threshold levels can be selected depending on the design requirements. Also, the constraint of a maximum battery power, for example 12 kW, was very well respected by the controller. The extra motor power required beyond the maximum battery power limit was supplied by the FC. Also, in Figure 8, a power split ratio of 1:6 was maintained wherever the two power sources contributed simultaneously to supplying the load demand. However, this ratio was violated when constraints were encountered. The controller was successful in determining the power set points of the FC and the battery with respecting the operational and safety constraints during tracking

the PSR. This good performance was achieved because the constraints were defined and embedded in the optimisation process.

The energy management was tested for short and long journeys. Simulations were performed for a powertrain consists of a battery of 12 kW rated power and a rated capacity of 20 kWh with a fuel cell of 20kW rated power and 2 kg hydrogen tank. It should be noticed that these values were not based on optimal sizing rather they were just chosen in order to investigate the controller performance against powertrain constraints of energy and power. A short journey of about 20 km was considered, which was estimated by the Sat-Nav to be 20 segments of different lengths. The controller in this case decided to supply all the power and energy demand solely from the battery, as shown in Figure 9. This was because the controller estimated the initial battery energy, represented as the SoC, to be enough to supply all the predicted energy demand over the journey. Such performance of dictating power priority can be attained by adaptively tuning the value of the weight factor w_3 to be very high compared to w_4. If for any reason during the journey the battery was unable to satisfy the motor load, then the MPC would update the current SoC and a decision would be made to draw additional power from the FC. Again, this can be achieved by returning w_3 to its original value.

For a long journey of about 100 km, two different constraints of final SoCs were tested. For a 20% final SoC limit, the controller estimated that there would be enough battery energy over the journey length. However, the energy requirement was different from the power requirement and therefore exceptions were made for the events where the maximum battery power was expected to be exceeded, as shown in Figures 10 and 11. The same long journey was tested again with a different final limit of 40% for SoC, see Figures 12 and 13. In this case, the controller realized that with this new constraint there would be a deficit in the battery energy and therefore the controller planned to dispatch FC power during the journey.

9 Conclusions

The controller was successful in applying the control objectives of battery power limits and threshold power for the FC. Also, the PSR was maintained wherever that was possible, considering the operational constraints. The performance indices in the cost function were designed to serve control objectives compatible with a plug-in powertrain configuration. Different powertrain configurations require introducing different performance indices and that will change the shape of the cost function and give different results.

Connecting the controller to an online map service and integrating the proposed control design to a real FCHEV powertrain system are planned as future work. This will also include extending the control algorithm to include the DC/AC inverter as a second control element to participate in controlling regenerative breaking events, and adding a supercapacitor to the system, requiring the introduction of new performance indices to consider a modified EMS considering regenerative breaking. As a future work as well, the costing of fuel cell energy can include the dependency on stack's efficiency. However, this will require a linear approximation of fuel cell power versus efficiency in order to keep the linear form of the cost function.

Applying the EMS to a real FCHEV is intended and will require substituting all the LabVIEW simulation loops with new loops that incorporate real-time measurements from sensors and transducers on-board the vehicle.

Acknowledgements

The authors would like to thank the conference committee of European Fuel Cell Forum (EFCF) 2019 for selecting this work to be included in a Special Issue in the Journal "Fuel Cells – From Fundamentals to Systems"

Appendix A:

The quadratic matrix $\boldsymbol{H}$:

$$\boldsymbol{H} = \begin{bmatrix} w_1\eta_c^{\,2} + w_3 & 0 & \cdots & 0 & 0 & 0 & 0 & \cdots & 0 & 0 \\ 0 & w_1\eta_c^{\,2} + w_3 & \cdots & 0 & 0 & 0 & 0 & \cdots & 0 & 0 \\ \vdots & \vdots & \ddots & \vdots & \vdots & \vdots & \vdots & \ddots & \vdots & \\ 0 & 0 & \cdots & w_1\eta_c^{\,2} + w_3 & 0 & 0 & 0 & \cdots & 0 & 0 \\ 0 & 0 & \cdots & 0 & w_1\eta_c^{\,2} + w_3 & 0 & 0 & \cdots & 0 & 0 \\ 0 & 0 & \cdots & 0 & 0 & w_2 + w_4 & 0 & \cdots & 0 & 0 \\ 0 & 0 & \cdots & 0 & 0 & 0 & w_2 + w_4 & \cdots & 0 & 0 \\ \vdots & \vdots & \ddots & \vdots & \vdots & \vdots & \vdots & \ddots & \vdots & \\ 0 & 0 & \cdots & 0 & 0 & 0 & 0 & \cdots & w_2 + w_4 & 0 \\ 0 & 0 & \cdots & 0 & 0 & 0 & 0 & \cdots & 0 & w_2 + w_4 \end{bmatrix}$$

The linear vector $\boldsymbol{f} = -\begin{bmatrix} w_1\left(P_{v*}^{k+1} - P_v^{id} + \varepsilon_{P_v}\right)\cdot\eta_c \\ w_1\left(P_{v*}^{k+2} - P_v^{id}\right)\cdot\eta_c \\ \vdots \\ w_1\left(P_{v*}^{k+N} - P_v^{id}\right)\cdot\eta_c \\ w_2\left(P_{v*}^{k+1} + P_v^{id} + \varepsilon_{P_v}\right) \\ w_2\left(P_{v*}^{k+2} + P_v^{id}\right) \\ \vdots \\ \vdots \\ w_2\left(P_{v*}^{k+N} + P_v^{id}\right) \end{bmatrix}$

Equality constraint:

$$\begin{bmatrix} \eta_c & 0 & \cdots & 0 & 0 & 1 & 0 & \cdots & 0 & 0 \\ 0 & \eta_c & \cdots & 0 & 0 & 0 & 1 & \cdots & 0 & 0 \\ \vdots & & \ddots & \vdots & & \vdots & & \ddots & \vdots & \\ 0 & 0 & \cdots & \eta_c & 0 & 0 & 0 & \cdots & 1 & 0 \\ 0 & 0 & \cdots & 0 & \eta_c & 0 & 0 & \cdots & 0 & 1 \end{bmatrix} \times \begin{bmatrix} P_{\mathrm{FC}}^{k+1} \\ P_{\mathrm{FC}}^{k+2} \\ \vdots \\ P_{\mathrm{FC}}^{k+N} \\ P_{\mathrm{B}}^{k+1} \\ P_{\mathrm{B}}^{k+2} \\ \vdots \\ P_{\mathrm{B}}^{k+N} \end{bmatrix} = \begin{bmatrix} P_{v*}^{k+1} \\ P_{v*}^{k+2} \\ \vdots \\ P_{v*}^{k+N} \end{bmatrix}$$

Inequality constraints:

$$\begin{bmatrix} \begin{bmatrix} 1 & 0 & \cdots & 0 & 0 \\ 0 & 1 & \cdots & 0 & 0 \\ \vdots & & \ddots & \vdots & \\ 0 & 0 & & 1 & 0 \\ 0 & 0 & \cdots & 0 & 1 \end{bmatrix} & \begin{bmatrix} 0 & 0 & \cdots & 0 & 0 \\ 0 & 0 & \cdots & 0 & 0 \\ \vdots & & \ddots & \vdots & \\ 0 & 0 & & 0 & 0 \\ 0 & 0 & \cdots & 0 & 0 \end{bmatrix} \\ \begin{bmatrix} -1 & 0 & \cdots & 0 & 0 \\ 0 & -1 & \cdots & 0 & 0 \\ \vdots & & \ddots & \vdots & \\ 0 & 0 & & -1 & 0 \\ 0 & 0 & \cdots & 0 & -1 \end{bmatrix} & \begin{bmatrix} 0 & 0 & \cdots & 0 & 0 \\ 0 & 0 & \cdots & 0 & 0 \\ \vdots & & \ddots & \vdots & \\ 0 & 0 & & 0 & 0 \\ 0 & 0 & \cdots & 0 & 0 \end{bmatrix} \\ \begin{bmatrix} 0 & 0 & \cdots & 0 & 0 \\ 0 & 0 & \cdots & 0 & 0 \\ \vdots & & \ddots & \vdots & \\ 0 & 0 & & 0 & 0 \\ 0 & 0 & \cdots & 0 & 0 \end{bmatrix} & \begin{bmatrix} 1 & 0 & \cdots & 0 & 0 \\ 0 & 1 & \cdots & 0 & 0 \\ \vdots & & \ddots & \vdots & \\ 0 & 0 & & 1 & 0 \\ 0 & 0 & \cdots & 0 & 1 \end{bmatrix} \\ \begin{bmatrix} 0 & 0 & \cdots & 0 & 0 \\ 0 & 0 & \cdots & 0 & 0 \\ \vdots & & \ddots & \vdots & \\ 0 & 0 & & 0 & 0 \\ 0 & 0 & \cdots & 0 & 0 \end{bmatrix} & \begin{bmatrix} -1 & 0 & \cdots & 0 & 0 \\ 0 & -1 & \cdots & 0 & 0 \\ \vdots & & \ddots & \vdots & \\ 0 & 0 & & -1 & 0 \\ 0 & 0 & \cdots & 0 & -1 \end{bmatrix} \\ \begin{bmatrix} t^1 & t^2 & \cdots & t^{N-1} & t^N \end{bmatrix} & \begin{bmatrix} 0 & 0 & \cdots & 0 & 0 \end{bmatrix} \\ \begin{bmatrix} 0 & 0 & \cdots & 0 & 0 \end{bmatrix} & \begin{bmatrix} t^1 & t^2 & \cdots & t^{N-1} & t^N \end{bmatrix} \end{bmatrix} \times \begin{bmatrix} P_{\mathrm{FC}}^{k+1} \\ P_{\mathrm{FC}}^{k+2} \\ \vdots \\ P_{\mathrm{FC}}^{k+N} \\ P_{\mathrm{B}}^{k+1} \\ P_{\mathrm{B}}^{k+2} \\ \vdots \\ P_{\mathrm{B}}^{k+N} \end{bmatrix} \leq \begin{bmatrix} \begin{bmatrix} 1 \\ 1 \\ \vdots \\ 1 \\ 1 \end{bmatrix} P_{FC}^{max} \\ \begin{bmatrix} 0 \\ 0 \\ \vdots \\ 0 \\ 0 \end{bmatrix} \\ \begin{bmatrix} 1 \\ 1 \\ \vdots \\ 1 \\ 1 \end{bmatrix} P_B^{\max} \\ \begin{bmatrix} 1 \\ 1 \\ \vdots \\ 1 \\ 1 \end{bmatrix} P_B^{min} \\ \begin{bmatrix} 1 \\ 1 \\ \vdots \\ 1 \\ 1 \end{bmatrix} \eta_{FC}\, \Delta H_{\mathrm{H_2}} \left(M_{\mathrm{H_2}}^{min} - M_{\mathrm{H_2}}^{0} \right) \\ \begin{bmatrix} 1 \\ 1 \\ \vdots \\ 1 \\ 1 \end{bmatrix} 3600\ C_{Wh} \left(SoC^{min} - SoC^{0} \right) \end{bmatrix}$$

List of Symbols

A_f	Vehicle frontal area / m^2
a	Vehicle acceleration / m s^{-2}
α	Battery efficiency term
C_d	Drag coefficient
C_{rr}	Rolling coefficient
C_{Wh}	Battery capacity / Wh
E	Nernst potential / V
E_0	Nernst potential / V
F	Faradays constant / C mol^{-1}
F_{aero}	Aerodynamic resistances / N

F_{grade}	Road gradient resistances / N
F_{rr}	Rolling resistances / N
F_i	Acceleration resistances / N
g	Gravitational acceleration / m s^{-2}
$\boldsymbol{f}$	linear vector of the quadratic equation
$\boldsymbol{H}$	Quadratic matrix
I_{FC}	FC current / A
i	Road segment number
$\boldsymbol{J}$	Cost function
k	Current time interval
N	Prediction horizon or total number of road segments
N_{cell}	No. of cell in FC stack
m	Vehicle mass / kg
M_{H_2}	Hydrogen inventory status / mole
$M_{H_2}^{min}$	Minimum hydrogen inventory / mole
$M_{\mathrm{H}_2}^{0}$	Initial Hydrogen inventory / mole
P_B	Battery power / W
$P_{B,sp}$	Battrey power set point / W
P_B^{max}	Maximum battery discharging power / W
P_B^{min}	Minimum battery power or maximum charging power / W
P_{FC}	FC power / W
$P_{FC,sp}$	FC power set point / W
P_{FC}^{max}	Maximum FC power / W
P_v	Vehicle power / W
P_{v*}	Prediction of vehicle power / W
P_v^{id}	Power shift parameter / W
$\vec{\mathbf{P}}_{\mathrm{FC}}$	Vector of FC power control variables
$\vec{\mathbf{P}}_{\mathrm{B}}$	Vector of battery power control variables
R	Gas constant, 8.314 / J K^{-1} mol^{-1}
ρ	Air density / kg m^{-3}
θ	Road angle / ^{o}
V_{FC}	FC voltage / V
v	Vehicle velocity / m s^{-1}
η_{act}	FC activation losses / V
η_{conc}	FC concentration losses / V
η_{ohm}	FC ohmic looses / V
η_{FC}	FC efficiency
η_c	DC-DC converter efficiency
η_{dis}	Battery discharging efficeicny
η_{ch}	Battery charging efficeicny
SoC	State of the charge of the battery

SoC^{min}	Minimum state of the charge of the battery
SoC^{max}	Maximum state of the charge of the battery
t	time / s
t_s	Sampling time / ms
w	Weighting factor
ε_{P_v}	Prediction error of vehicle power / W

References

[1] G. J. Offer, D. Howey, M. Contestabile, R. Clague, N. P. Brandon, *Energy Policy* **2010**, *38*, 24–29.

[2] C. M. Martinez, X. Hu, D. Cao, E. Velenis, B. Gao, M. Wellers, *IEEE Transactions on Vehicular Technology* **2017**, *66*, 4534–4549.

[3] N. Denis, M. R. Dubois, P. F. Trov, S. Member, A. Desrochers, *IEEE Transactions on Vehicular Technology* **2018**, *67*, 315–326.

[4] J. Fan, J. Zhang, T. Shen, *Energies* **2015**, *8*, 9946–9968.

[5] M. F. M. Sabri, K. A. Danapalasingam, M. F. Rahmat, *Renewable and Sustainable Energy Reviews* **2016**, *53*, 1433–1442.

[6] C. Bordons, M. a. Ridao, A. Perez, A. Arce, D. Marcos, in *IEEE Vehicle Power and Propulsion Conference* (Eds.: E. Ali, S. John, J. Economou, M. Ehsani), Lille, France, **2010**, pp. 1-6.

[7] C. Sun, S. J. Moura, X. Hu, J. K. Hedrick, F. Sun, *IEEE Transactions on Control Systems Technology* **2015**, *23*, 1075–1086.

[8] L. Guzzella, A. Sciarretta, *Vehicle Propulsion Systems: Introduction to Modeling and Optimization*, Springer, Berlin, **2005**, pp. 13-21.

[9] E. Kim, J. Lee, K. G. Shin, in *Proceedings of the ACM/IEEE 4th International Conference on Cyber-Physical Systems - ICCPS '13* (Eds.: C. Lu, P.R. Kumar, R. Stoleru), ACM Press, New York, New York, USA, **2013**, pp. 11-20.

[10] EV Trip Planner, can be found under https://www.evtripplanner.com/index.php, **2019**.

[11] J. Wilhelm, in *Fuel Cell Science and Engineering: Materials, Processes, Systems and Technology* (Eds.: D. Stolten, B. Emonts), Wiley-VCH Verlag, Weinheim, Germany, **2012**, pp. 1075-1103.

[12] F. Barbir, *PEM Fuel Cells: Theory and Practice*, Academic Press Inc, San Diego, United States, **2005**, pp. 39.

[13] J. Larminie, A. Dicks, *Fuel Cell Systems Explained*, John Wiley & Sons, Ltd,., West Sussex, **2003**, pp. 45.

[14] C. Xie, J. M. Ogden, S. Quan, Q. Chen, *International Journal of Electrical Power and Energy Systems* **2013**, *53*, 307–320.

[15] M. Z. Daud, A. Mohamed, M. A. Hannan, *Energy Conversion and Management* **2013**, *73*, 256–270.

[16] P. Garcia, J. P. Torreglosa, L. M. Fernandez, F. Jurado, *Expert Systems with Applications* **2013**, *40*, 4791–4804.

[17] M. Toman, R. Cipin, D. Cervinka, P. Vorel, P. Prochazka, *ECS Transactions* **2016**, *74*, 37–43.

[18] X. Li, D. Hui, X. Lai, *IEEE Transactions on Sustainable Energy* **2013**, *4*, 464–473.

[19] K. Li, K. J. Tseng, in *IECON - 41st Annual Conference of the IEEE Industrial Electronics Society*, Yokohama, Japan, **2015**, pp. 5235-5240.

[20] J. A. Rossiter, *Model- Based Predictive Control: A Practical Approach*, CRC Press Inc, Bosa Roca, **2003**, pp. 5.

[21] G. Morrison, J. Stevens, F. Joseck, *Transportation Research Part C: Emerging Technologies* **2018**, *87*, 183–196.

[22] I. Evtimov, R. Ivanov, M. Sapundjiev, in *BulTrans - 9th International Scientific Conference on Aeronautics, Automotive and Railway Engineering and Technologies* (Eds.: B. Gigov, N. Nikolov, V. Stoilov, M. Todorov), Sozopol, Bulgaria, **2017**, pp. 1.

[23] E. F. Camacho, C. Bordons, *Model Predictive Control*, Springer Ltd, London, United Kingdom, **2007**, pp. 1.

Figure Captions

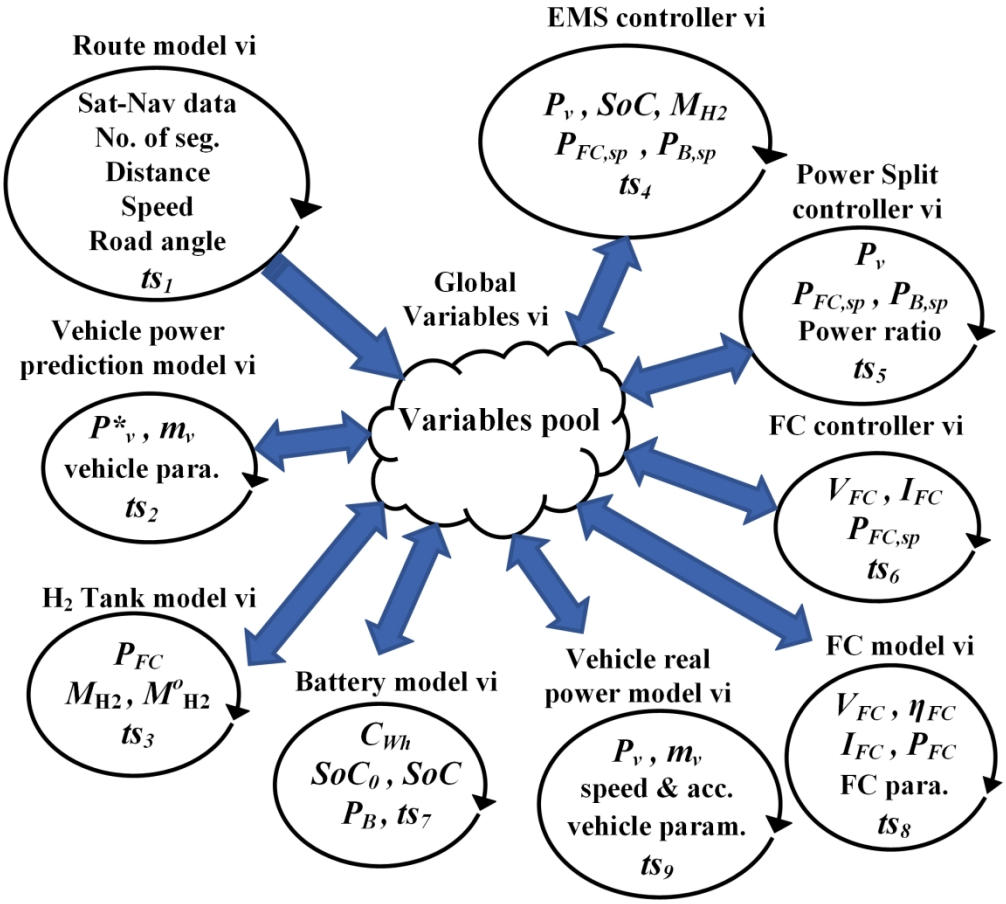

Figure 1: Simulation architecture based on multiple LabVIEW vi drivers

172x155mm (300 x 300 DPI)

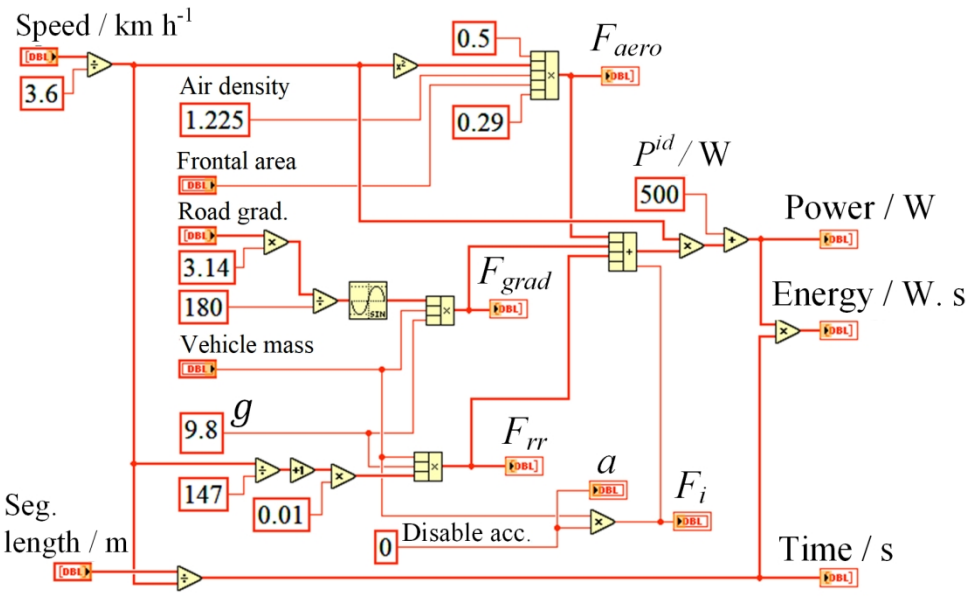

Figure 2 LabVIEW model for power and energy prediction of the vehicle

159x96mm (300 x 300 DPI)

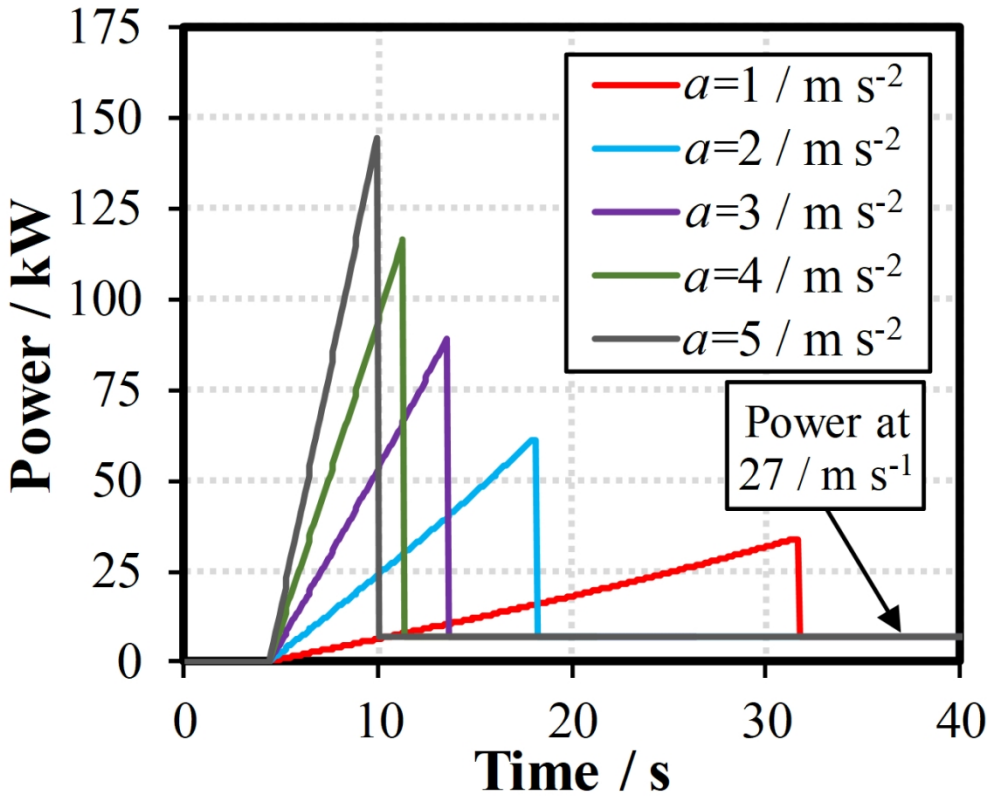

Figure 3: Vehicle power profiles at different accelerations from rest to a speed of 27 m s^{-1}

83x67mm (400 x 400 DPI)

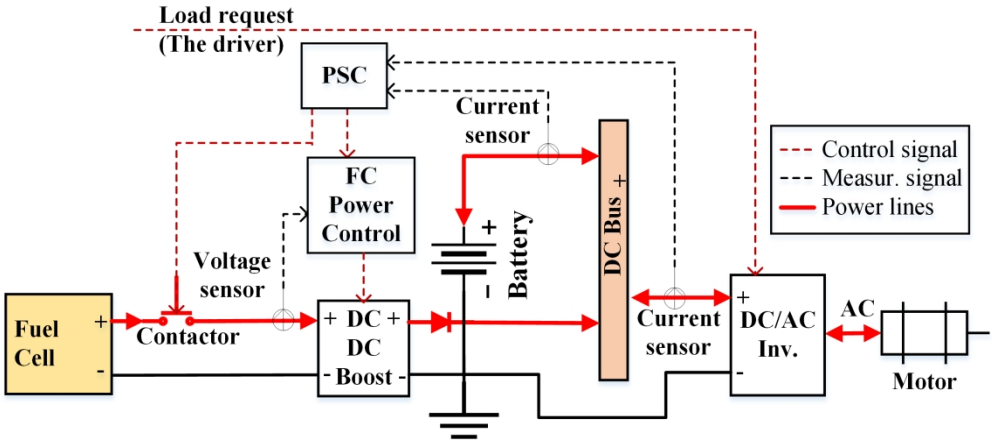

Figure 4: FCHEV powertrain design

176x78mm (400 x 400 DPI)

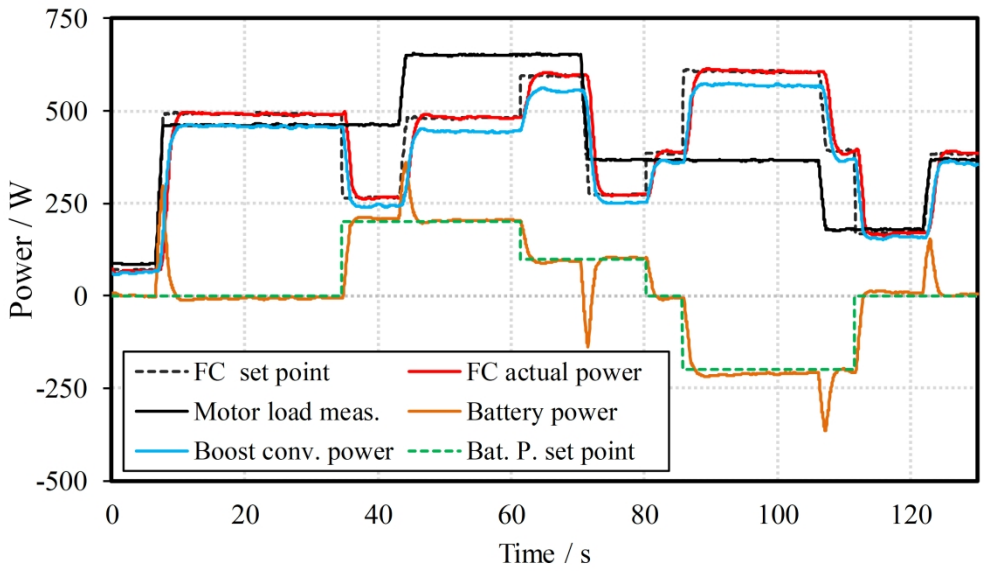

Figure 5: Low-level power split controller performance

172x100mm (400 x 400 DPI)

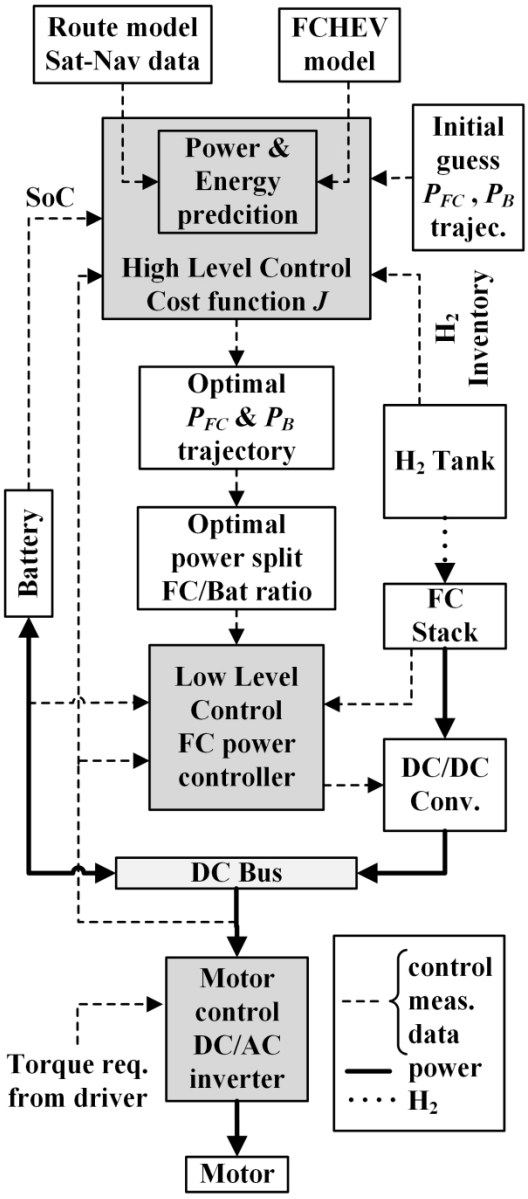

Figure 6: MPC algorithm of energy management control of FCHEV

83x181mm (400 x 400 DPI)

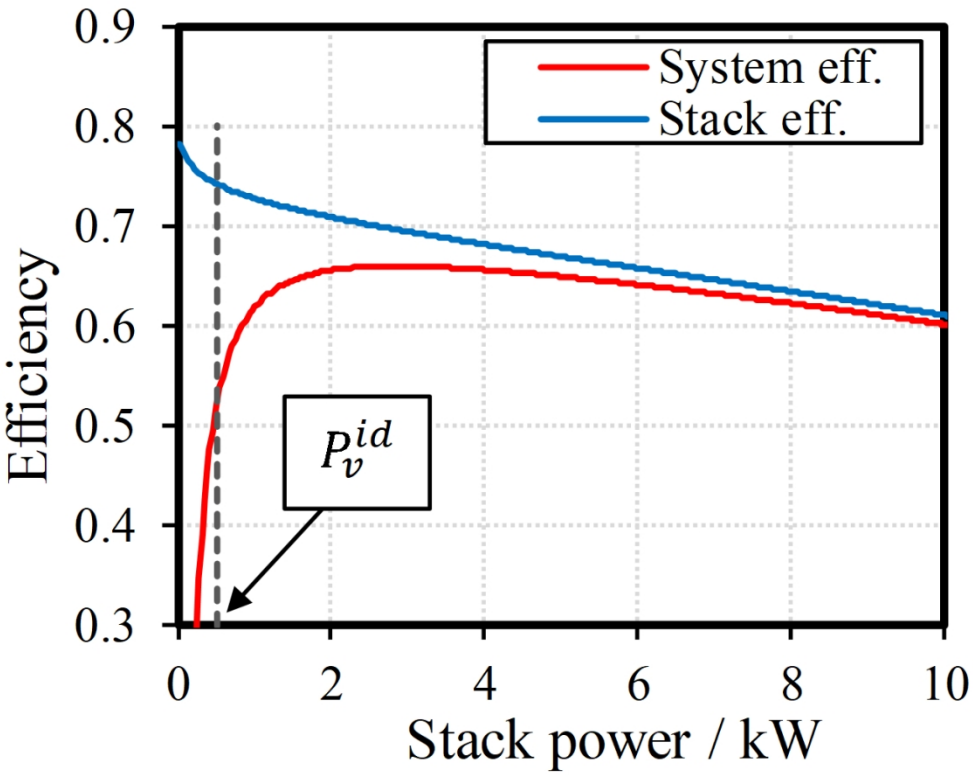

Figure 7: FC system and stack efficiencies

84x65mm (400 x 400 DPI)

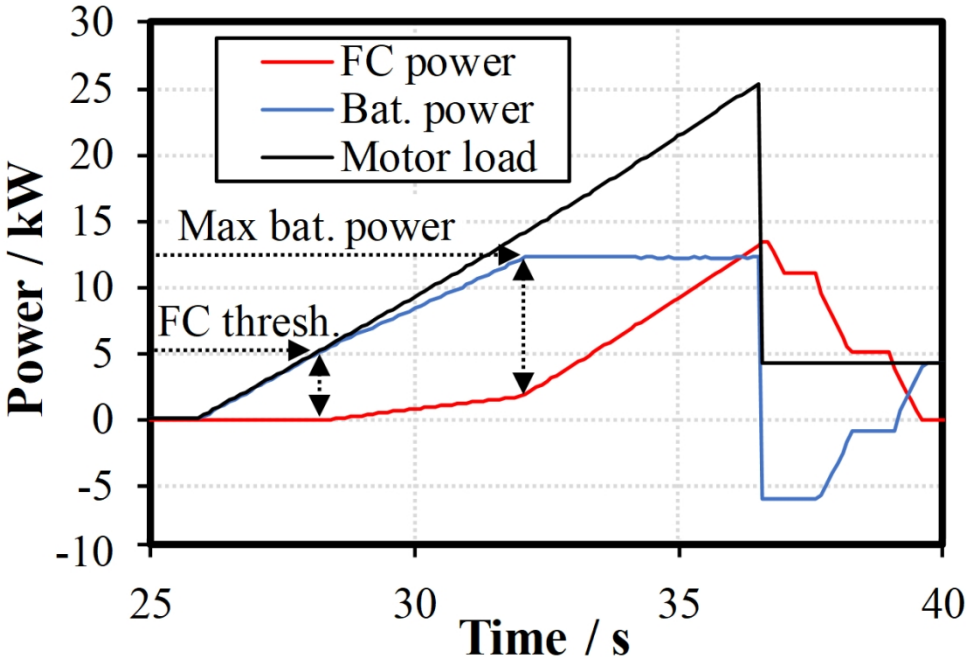

Figure 8: Controller response at FC threshold power and maximum battery power

83x56mm (400 x 400 DPI)

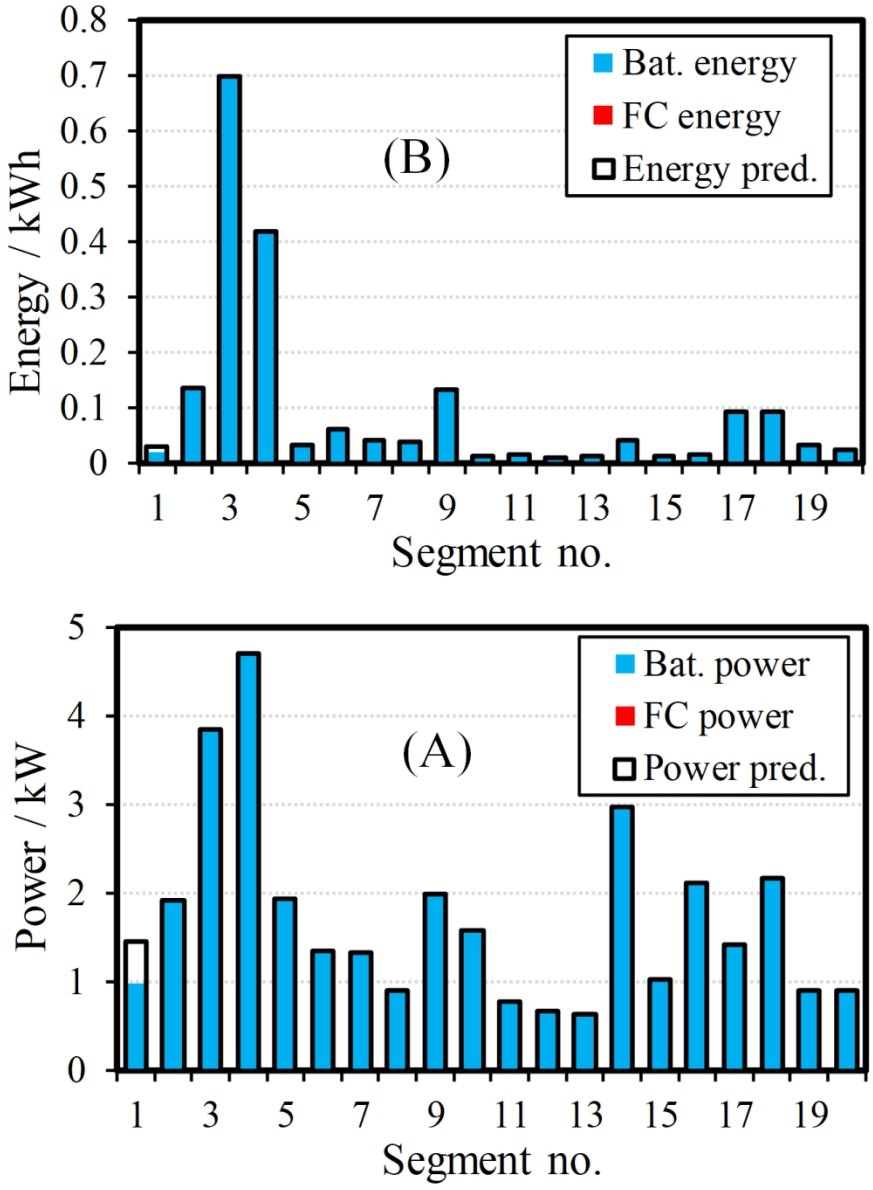

Figure 9: (A) Power management and (B) energy management for a short journey

86x115mm (400 x 400 DPI)

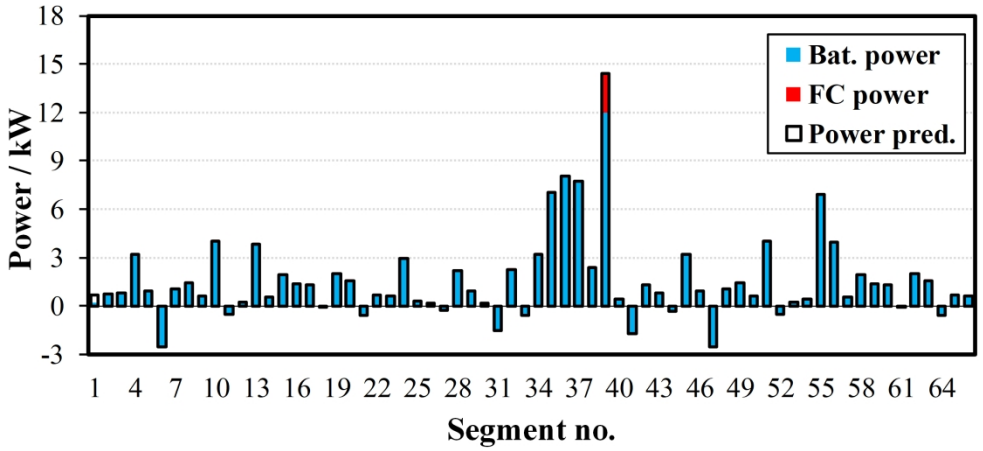

Figure 10: Power management for a long journey with a final SoC limit of 20%

173x79mm (400 x 400 DPI)

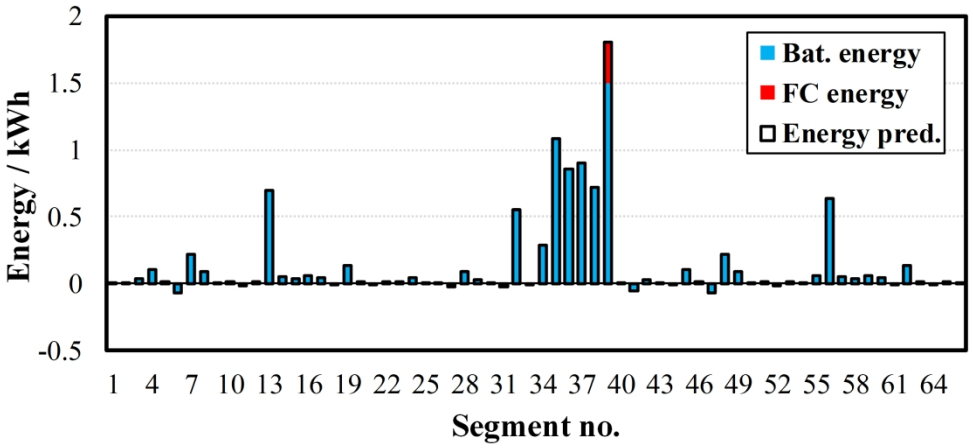

Figure 11: Energy management for a long journey with a final SoC limit of 20%

173x79mm (400 x 400 DPI)

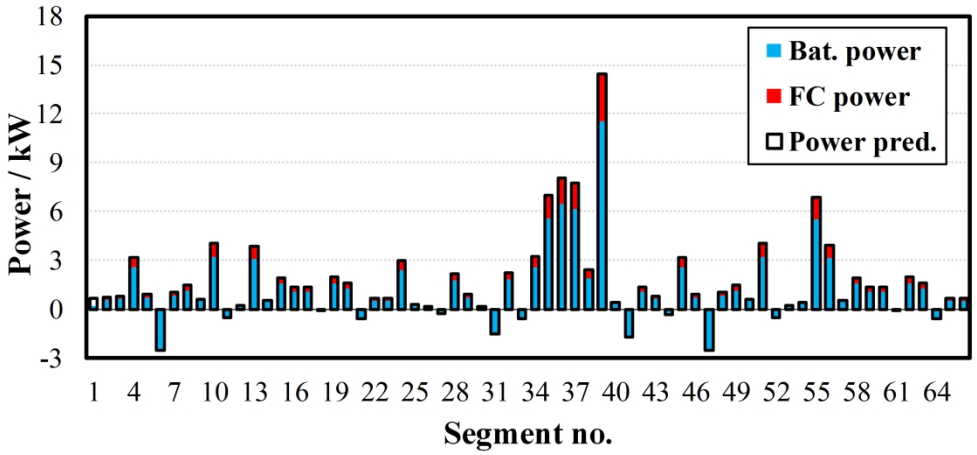

Figure 12: Power management for a long journey with a final SoC limit of 40%

172x79mm (400 x 400 DPI)

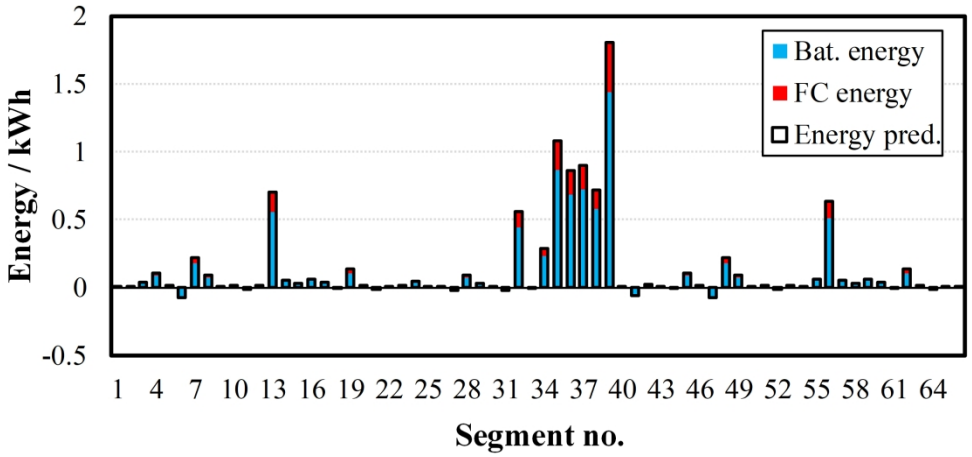

Figure 13: Energy management for a long journey with a final SoC limit of 40%

172x79mm (400 x 400 DPI)